# MSEC2023-103829

Roza Vavari

# PHYSICS-BASED FEEDFORWARD CONTROL OF THERMAL HISTORY IN LASER POWDER BED FUSION ADDITIVE MANUFACTURING

7ivad Smoai

Virginia Tech	Virginia Tech		University of Nebraska		Vulcan Forms
Blacksburg, VA	Blacksburg, VA		Lincoln, NE		Burlington, MA
Ajay Krishnan Edison Welding Institute Columbus, OH	Josie Gilligan Lincoln Public Schools Lincoln, NE	<b>Nicholas Piercy</b> University of Nebraska Lincoln, NE		<b>Kevin Cole</b> University of Nebraska Lincoln, NE	<b>Prahalada Rao</b> Virginia Tech Blacksburg, VA

Ranjamin Rayans

#### **ABSTRACT**

We developed and applied a model-based feedforward control approach to reduce temperature-induced flaw formation in the laser powder bed fusion (LPBF) additive manufacturing process. The feedforward control is built upon three basic steps. First, the thermal history of the part is rapidly predicted using a mesh-free graph theory model. Second, thermal history metrics are extracted from the model to identify regions of heat buildup. symptomatic of flaw formation. Third, process parameters are changed layer-by-layer based on insights from the thermal model. This technique was validated with two identical build plates (Inconel 718). Parts on the first build plate were made under manufacturer recommended nominal process parameters. Parts on the second build plate were made with model optimized process parameters. Results were validated with in-situ infrared thermography, and materials characterization techniques. Parts produced under controlled processing exhibited superior geometric accuracy and resolution, finer grain size, and increased microhardness.

Alay Rianscha

Keywords: Rapid Prototyping and Solid Freeform Fabrication, Welding and Joining, Control and Automation, Modeling and Simulation

#### 1. INTRODUCTION

The goal of this work is to develop and apply a feedforward control optimization approach for reducing temperature-based flaw formation in the laser powder bed fusion (LPBF) process. Temperature predictions from a physics-based thermal simulation model are used to alter process parameters layer by layer before printing in order to avoid heat buildup and reduce flaw formation as a result.

In LPBF, metal powder is raked onto a build plate and selectively melted using an infrared laser. While the process allows unparalleled freedom of design and offers the capability to reduce lead times, the process has yet to be accepted by the wider industry. One critical issue that prevents widespread adoption is the processes tendency to create flaws, which causes variation in the resulting part properties [1,2].

Flaw formation in LPBF is caused by the temperature distribution in the part during the process, commonly called the thermal history. Multiple flaw formation modes are linked to the thermal history, including recoater crash, support collapse, distortion and cracking, and inconsistent microstructure [1,3–5].

Thermal history of LPBF parts is influenced by a number of factors, including part shape, build layout, processing parameters and material feedstock [5,6]. Due to the layer-by-layer nature of the LPBF process, the thermal history of LPBF parts will vary substantially [4]. As a result, using empirically optimized process parameter can still result in flaw formation in parts. Hence, for complex geometries while some flaws, such as porosity, may be eliminated by traditional process optimization, others flaws, e.g., distortion or microstructure heterogeneity may manifest [1].

In this work a physics-based process parameter optimization approach is used to mitigate flaw formation in LPBF parts. The main idea is to reduce heat buildup by altering process parameters on a layer-by-layer basis before the part is started based on predictions from a thermal model. This feed forward process control approach is stratified into three steps, as shown in FIGURE 1,

- 1: <u>Predict</u> the thermal history of the part using a rapid graph theory based thermal model.
- 2: <u>Analyze</u> the modeled thermal history trends and identify layers where excessive heat buildup is predicted to occur. The thermal history is represented as end-of-cycle temperature, which is the surface temperature of the part after a layer is completed. The aim is to minimize the difference (slope) in end-of-cycle temperature between layers.

3: <u>Correct</u> the heat buildup in the identified layers through use of process parameter changes. In this work, laser power and dwell time between layers were altered. The magnitude of process parameter changes and layers at which they are initiated are obtained thorough iterative simulation.

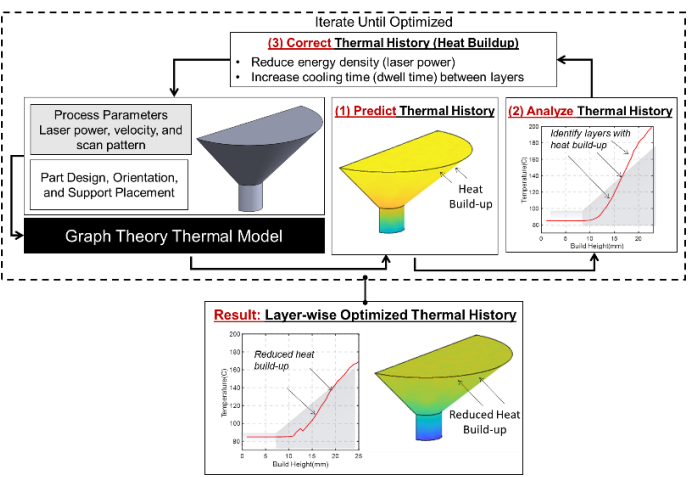


**FIGURE 1:** MODEL-DRIVEN FEED FORWARD CONTROL APPROACH CONSISTS OF THREE STEPS. (STEP 1) PREDICTION OF THERMAL HISTORY USING THE GRAPH THEORY. (STEP 2) ANALYSIS OF THE PREDICTED THERMAL HISTORY TRENDS TO IDENTIFY HEAT BUILDUP. (STEP 3) CORRECTION OF HEAT BUILDUP BY ADJUSTING PROCESS PARAMETERS LAYER-BY-LAYER THROUGH ITERATIVE SIMULATION.

This process is unique in the fact that it does not require sensor information to change the process state. Instead process changes are made before the part is printed in a feedforward arrangement. Because feedforward models are proactive in nature, they can prevent flaw formation from systemic flaw formation causes, where feedback is forced to react to flaw formation once flaw formation begins.

# 2. MATERIALS AND METHODS2.1 Experimental Setup

Parts were manufactured in partnership with Edison Welding Institute (EWI) on their open architecture system. The system allows critical processing parameters, including laser power, velocity, hatch spacing, dwell time, etc., to be altered through GCODE. A long wave infrared thermal camera was used to measure the end-of-cycle surface temperature, or the temperature of parts before a subsequent laser strike of the parts as they were built. The thermal camera was calibrated to accurately measure temperatures between 0 °C and 250 °C using a black-body technique used in our previous works [4,7]. This temperature data serves as a means for validating the thermal model. A schematic of the experimental setup is provided in FIGURE 2. The camera was located 80° from the horizontal in such a way that the camera is capable of capturing the entire build plate within the field of view, enabling analysis of the entire top surface of each layer during the build.

Two build plates were created in this work. Both build plates have identical parts placed in identical locations on the build plate. Parts were spaced in such that at least 10 mm spacing was kept between all parts. Both builds were made with the same lot of Inconel 718 powder. The build plate design can be observed in FIGURE 3. The first build plate was created using nominal process conditions (285 W laser power, 960 mm/sec scan speed, 40  $\mu$ m layer height, 110  $\mu$ m hatch spacing). The second build plate was used with process conditions prescribed by the feedforward control of this work. In total 16 parts were created on each build plate, with 10 unique geometry designs.

Two representative parts were selected for analysis in this work, termed cone and vase. These parts were selected as they were conducive for metrology and post-process characterization. The specific design intents for each part are described in FIGURE 3, along with the characterization completed.

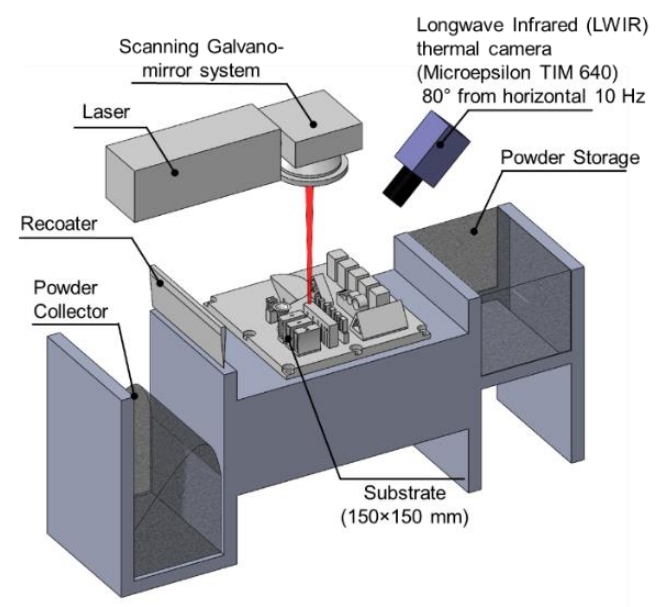


**FIGURE 2:** SCHEMATIC OF LPBF SYSTEM WITH AN INFRARED CAMERA TO OBSERVE THE TOP SURFACE OF EACH LAYER OF THE BUILD.

#### 2.2 Post-Process Characterization

Parts were examined post-process using both non-destructive and destructive characterization techniques. Before destructive techniques were conducted, non-destructive techniques were used including X-ray computed tomography (XCT), Archimedes relative density measurement, and laser scanning surface roughness microscopy. X-ray scanning was conducted with a 10 µm voxel resolution. This provided geometric deviation and porosity analysis. The porosity results were validated with Archimedes relative density measurements.

After non-destructive evaluation, the parts were cross sectioned using wire electro-discharge machining. The surfaces of the parts were polished and etched in order to image the microstructure using optical and scanning electron microscopy.

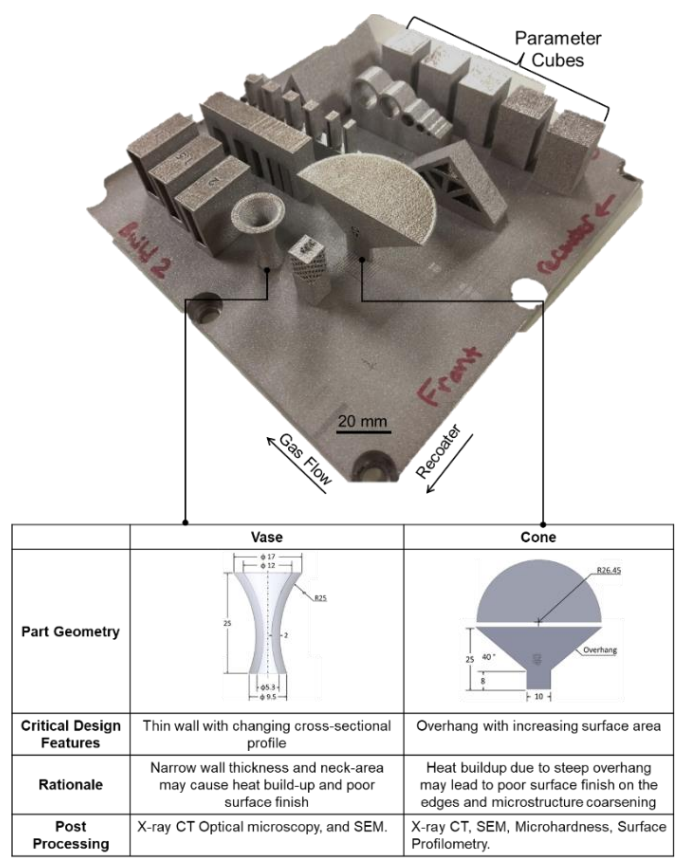


**FIGURE 3:** (ABOVE) COMPLETED BUILD PLATE WITH ALL GEOMETRIES CREATED IN THIS WORK. (BELOW) SELECTED PARTS FOR THIS PUBLICATION AND THE RATIONALE FOR EACH GEOMETRY.

### 2.3 Graph Theory Modeling and Validation

A critical component of this work is the prediction of thermal history using the graph theory thermal model. The graph theory approach solves the heat diffusion equation for each point (x,y,z) at a point in time (t) [8,9]. The thermal history T(x,y,z,t) is obtained as.

$$\rho c_p \frac{\partial T(x,y,z,t)}{\partial t} - k \underbrace{\left(\frac{\partial^2}{\partial x^2} + \frac{\partial^2}{\partial y^2} + \frac{\partial^2}{\partial z^2}\right)}_{Laplacian operator} T(x,y,z,t) = Q \qquad (1)$$

By replacing the continuous Laplacian operator in the foregoing equation with a discrete Laplacian matrix (L) motivated from graph theory, the equation is solved as a function of eigenvalues and eigenvectors of L as follows,

$$T(x, y, z, t) = \phi e^{-\alpha g \Lambda t} \phi' T_0(x, y, z)$$
 (2)

Further, to accommodate the alteration of process parameters, the initial temperature of the meltpool is assumed to change linearly with laser power within the practical laser regime. The resulting initial temperature function is altered to take the form,

$$T_0(x, y, z) = T_{\text{nom}} \times \frac{P_{\text{new}}}{P_0} \beta$$
 (3)

Where  $T_{nom}=1600~^{\circ}C$  is the assumed melting temperature of nickel alloy 718 at the nominal laser power of  $P_0=285~W$ ;  $P_{new}$  is the altered laser power from the feedforward process control, and  $\beta=0.95$  is a constant which was determined by model calibration.

Previous work has shown that this model is capable of accurately modeling 3D heat transfer problems which have an analytical solution. The method is capable of showing a less than 1% error while computing the solution 2.5 to 5 times faster than commercial finite element solutions [10,11]. This has also been shown to provide comparable results to commercial LPBF simulation software and experimental data. These works confirm that the model can converge to the same solution in 1/10<sup>th</sup> of the time of non-proprietary models with similar levels of error [12,13].

To validate the results of the model, a thermal metric called end-of-cycle temperature was extracted from the top surface temperature of each part layer. The temperature of the layer after the lasing of a single layer is completed was extracted from the IR camera and the thermal model and the results were compared.

The process for obtaining end-of-cycle temperature is depicted in FIGURE 4. In order to obtain end-of-cycle temperatures, a region of interest was identified, and is shown in the cross section of FIGURE 4(a). In this work, a 3×3 pixel (60 μm × 60 μm) region of interest was identified for all parts. By averaging this region for each layer, the entire temperature history is shown in FIGURE 4(b). An additional detailed view is shown in FIGURE 4(c). In this view, the laser strike is observed on each new layer as a large temperature spike. Because the IR camera was calibrated for the part being covered in powder, the recoater cycle appears as a small rise after the laser strike. By extracting the temperature just before the laser strike at the point labeled (B), the end-of-cycle temperature for that layer can be extracted. FIGURE 4(d) shows the resulting end-of-cycle temperature for each layer of the cone-shaped part under standard processing conditions.

In previous work, end-of-cycle temperature has been shown to correlate to gross part distortion and recoater crash [4]. From the example shown in FIGURE 4, it is possible to observe the rapid rise in the end-of-cycle temperature once the overhang of the cone shape begins. This is easily explained by the increasing cross section area and the limited contact to the build plate for heat dissipation. These sudden increases in the temperature of the parts are what this work seeks to avoid, as these sudden rises are hypothesized to create defects in parts.

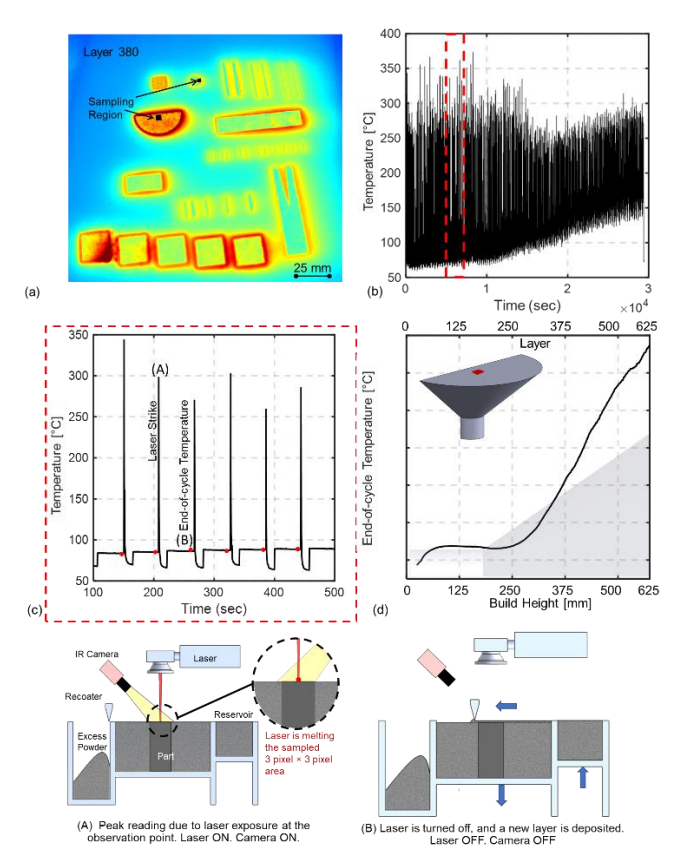


**FIGURE 4:** PROCESS OF OBTAINING END-OF-CYCLE TEMPERATURE FROM IR DATA. A SAMPLE REGION IS SELECTED FOR EACH PART, WHICH IS CONCATENATED INTO A TIME SERIES. BY SELECTING THE POINT JUST BEFORE THE LASER STRIKES THIS POINT(B,C), THE END-OF-CYCLE TEMPERATURE CAN BE EXTRACTED(D).

# 2.4 Process Parameter Selection and Control

As mentioned in the context of FIGURE 1, the feedforward control approach was divided into three steps. These steps are denoted as predict, analyze, and correct.

In the first step, the thermal history of the desired geometry is predicted using the graph theory thermal model. Subsequently, regions of potential heat buildup are identified. In this work increases in temperature greater than 20 °C between successive layers were considered points of significant heat buildup that should be mitigated by changing the process parameters. This threshold was determined from previous work showing that steep rises in thermal history over 20 °C/layer result in severe distortion and recoater crashes [4]. The parts are then simulated iteratively with various process parameter combinations.

By applying the feedforward control approach to this work, a new set of process parameters were obtained. To ease practical implementation, each part was limited to one laser power change for each part, as these changes were manually implemented in the build GCODE. In addition, laser power was the only parameter that could be adjusted for each part. The resulting laser power changes and global dwell time changes recommended by the feedforward control process are summarized in FIGURE 5.

As an example, in FIGURE 4(d), the expected temperature of the cone-shaped part expressed a rapid heat buildup at 12 mm of build height. As a result, the feedforward control technique recommended a reduction in the laser power from the nominal 285 W to 200 W. Due to the model being unable to fully control the thermals with laser power, a 10 second dwell time was added to the controlled build in order to further control heat buildup.

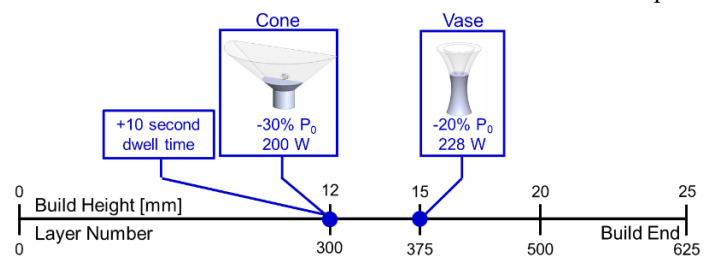


**FIGURE 5:** SUMMARY OF THE PROCESS PARAMETERS ADJUSTED BY CONTROLLED PROCESSING OF THE TWO PARTS. ONCE LASER POWER IS ADJUSTED, IT IS MAINTAINED UNTIL THE END OF THE BUILD.

The control bounds for laser power is limited to prevent lack-of-fusion and keyholing porosity regimes from affecting the build. For this work, the laser power was determined to by maintained at  $\pm 30\%$  of the nominal laser power of 285 W to prevent the process from entering the keyhole or lack-of-fusion regime. This means that the laser power alterations were limited between 200 W and 380 W. These boundaries were based analysis from five parameter cubes made on the standard build plate. These cubes were created with processing parameters between 185 W laser power and 385 W laser power. Porosity analysis was conducted using Archimedes relative density measurement, which provided a relative density for each cube. The relative density was validated by XCT, which provides defect volume ratio (DVR), which is the ratio of porosity volume over the total part volume. The results of this analysis are shown in FIGURE 6, which shows that below laser power of 200 W, the relative density of the cubes decreases rapidly.

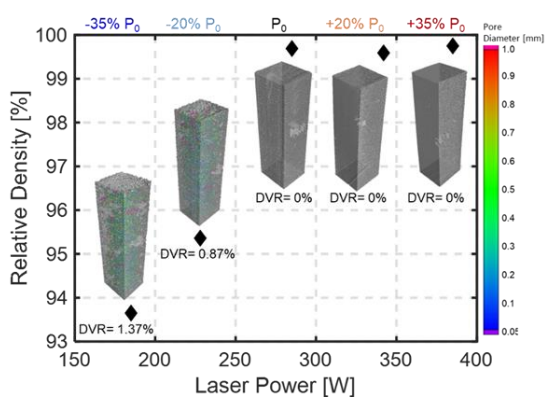


**FIGURE 6:** RELATIVE DENSITY MEASUREMENT FOR THE DENSITY CUBES. LOW ENERGY TENDS TO CREATE LACK OF FUSION DEFECTS.

### 3. RESULTS AND DISCUSSION

#### 3.1 Cone

The predicted thermal history and the IR measured end-of-cycle temperature are compared in FIGURE 7 for both the fixed and controlled build plates. The graph theory model was repeated for 10 runs to quantify run-to-run variation. The significant increase in end-of-cycle temperature as accurately quantified by the thermal model for the fixed condition case, and the controlled case accurately predicted the reduction in heat buildup. The model prediction error was within 2%, and the simulation converged in less-than 5 minutes on a desktop computer.

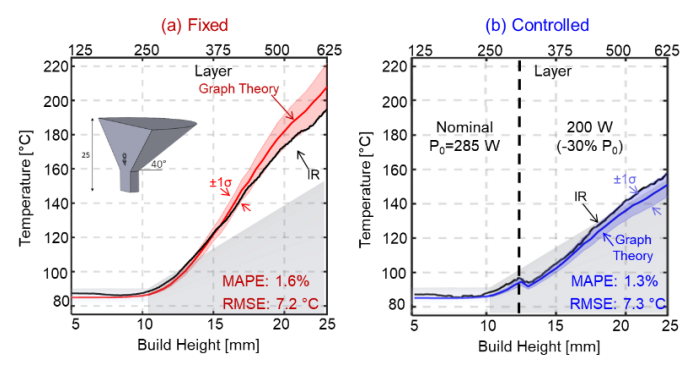


**FIGURE 7:** PREDICTED SURFACE TEMPERATURE TRENDS COMPARED TO IR MEASUREMENTS FOR THE (A) FIXED AND (B) CONTROLLED PROCESSED INVERTED CONE. THE SIMULATION TIME WAS 2 MINUTES.

While the end-of-cycle temperature measurement details one point of the build, the alteration of process parameters affected the entire part thermal history. FIGURE 8 shows the difference between the predicted thermal history for the standard and controlled processing conditions. Because the process alteration affected the entire layer, the total part heat buildup was reduced, especially near the top and end of the build as the cross-sectional area increased.

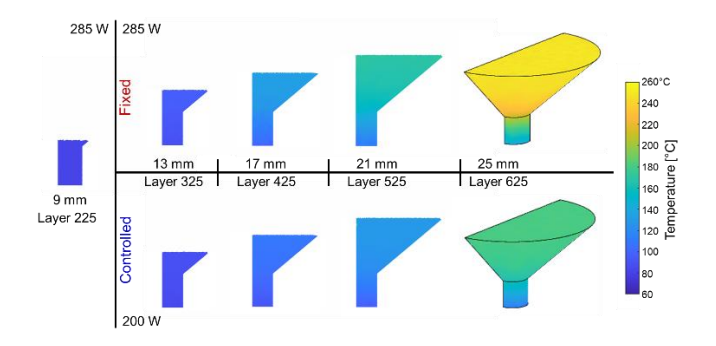
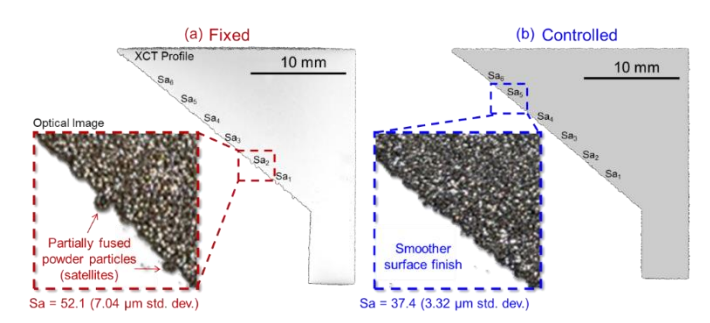


FIGURE 8: SPATIAL TEMPERATURE DISTRIBUTION FOR THE CONE PART PREDICTED USING THE GRAPH THEORY THERMAL MODEL FOR FIXED PROCESSING (TOP) AND CONTROLLED PROCESSING (BOTTOM). IN CONTROLLED PROCESSING HEAT BUILDUP AND SPATIAL TEMPERATURE GRADIENTS ARE SIGNIFICANTLY REDUCED BY DECREASING THE LASER POWER TO 200 W FROM LAYER 300 ONWARDS.

Controlled processing resulted in several improvements to part properties. First, as shown in FIGURE 9 the areal surface roughness (Sa) over the overhang region was reduced in the controlled part. For the controlled part the Sa  $\approx 37~\mu m$  compared to Sa  $\approx 52~\mu m$  for the standard-processed part.

The effect of the thermal history alteration on the microstructure evolved is evident in FIGURE 10, which shows the etched cross sectioned views of the microstructure. The difference in grain size is immediately apparent and was confirmed by measuring the primary dendritic arm spacing  $(\lambda_1)$  between the two parts.



**FIGURE 9:** X-RAY CT AND OPTICAL IMAGES OF THE CONESHAPED PARTS. (A) FIXED PROCESSING RESULTED IN A ROUGHER SURFACE FINISH (SA  $\approx 52~\mu\text{M}$ ) DUE TO PARTIALLY FUSED PARTICLES (SATELLITES) ATTACHED TO THE OVERHANG EDGE. (B) CONTROLLED-PROCESSED CONE HAS A SMOOTHER SURFACE FINISH (SA  $\approx 37~\mu\text{M}$ ) WITHOUT SATELLITE PARTICLES.

To measure primary dendritic arm spacing  $(\lambda_l),~20~\mu m$  regions were selected perpendicular to the dendrite growth direction. As shown in FIGURE 10(c), where the processing parameters were the same, the primary dendritic arm spacing is identical. Where the processing parameters were changed in the with the feedforward control process, the grain size reduces  $(\lambda_l$  decreases). The  $\lambda_l$  for the standard processed cone was  $\lambda_l\approx 0.69$   $\mu m\pm 0.02~\mu m$ , whereas the controlled processed cone had a  $\lambda_l\approx 0.49~\mu m\pm 0.02~\mu m$ . This difference in grain size resulted in a differences in the microhardness of the parts; evident in FIGURE 10(d), for the controlled-processed parts the average microhardness increased from  $HV_{05}\sim 290$  to  $HV_{05}\sim 320$ .

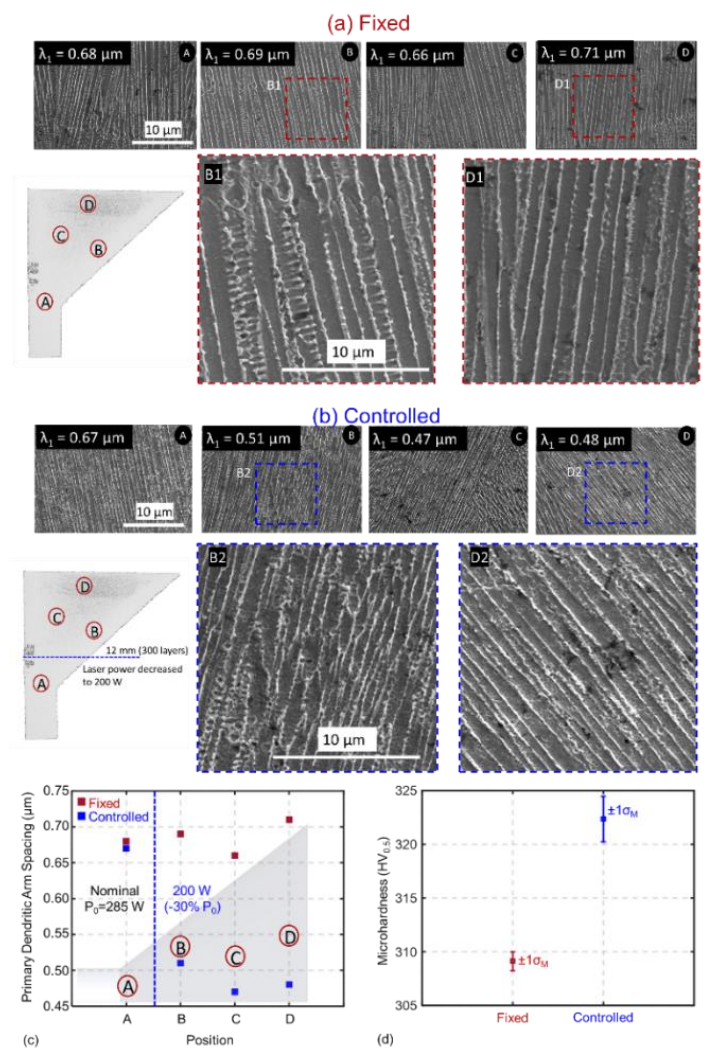
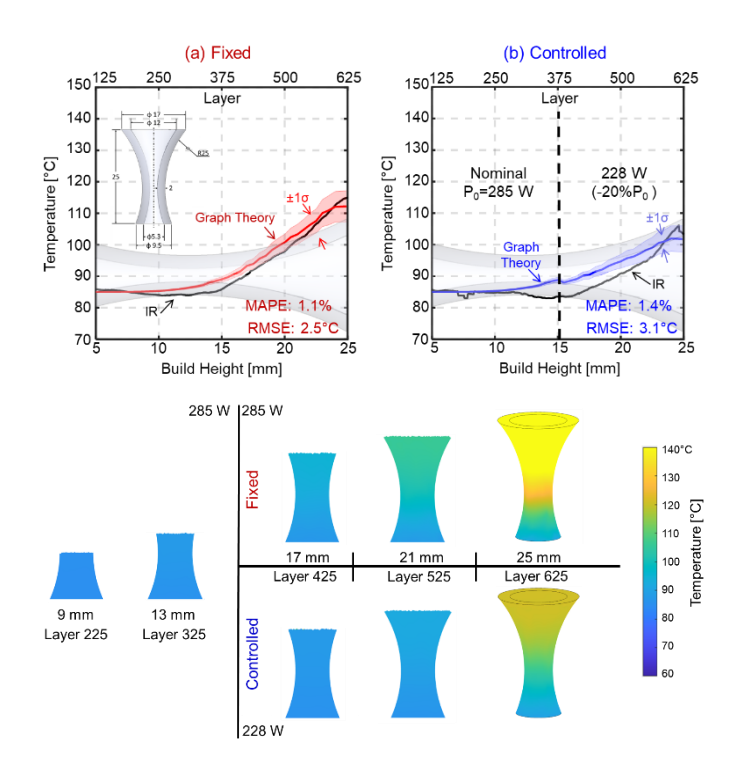


FIGURE 10: MICROSTRUCTURE COMPARISON OF CONE PARTS CREATED UNDER FIXED (A) AND CONTROLLED (B) PROCESSING CONDITIONS. (C) PRIMARY DENDRITIC ARM SPACING AS A FUNCTION OF BUILD HEIGHT. (D) MICROHARDNESS COMPARISON BETWEEN THE FIXED AND CONTROLLED PROCESSED CONE.

## 3.2 Vase

The predicted and IR-measured end-of-cycle surface temperature measurements are presented in FIGURE 11. The heat buildup predicted beyond layer 375 was mitigated in the feedforward approach by reducing the laser power to 228 W until the build concluded. The graph theory thermal model predicted the thermal history for both the standard and controlled geometries with error less-than 2% within 3 minutes. As evident from FIGURE 11 (bottom), as the part builds up, controlled processing reduces the heat buildup in the bulk section.



**FIGURE 11:** (TOP) PREDICTED SURFACE TEMPERATURE TRENDS COMPARED TO IR MEASUREMENTS FOR THE (A) FIXED AND (B) CONTROLLED PROCESSED INVERTED VASE. (BOTTOM) THE 3D TEMPERATURE DISTRIBUTION FOR FIXED AND CONTROLLED PROCESSING.

While the difference in temperature was less than the cone parts, the thin walls and increased geometric complexity resulted in a pronounced effect on the integrity of the part. FIGURE 12 shows an optical micrograph comparison of the neck region of the two parts after cross sectioning. In the standard-processed case, the central cavity was fused shut by oversintering of surrounding powder. By implementing the feedforward control approach, oversintering was reduced, and the cavity was open.

To further quantify the improvement in geometric accuracy, XCT volume scans were compared to the nominal CAD file used to create the vase geometry. The resulting nominal/actual geometry comparison is presented in FIGURE 12, with outward (positive) deviation presented as red. Geometric deviation was observed on the inside and outside of the vase for the fixed-processed part was greater than 0.1 mm on both the inner and outer surfaces of the part. By contrast, the controlled processed vase part maintained its geometric integrity and was closer to the nominal part design.

As with the cone, altering the laser power on a fixed layer will substantially alter the thermal history of the layers below it. This effect is apparent in FIGURE 11. This observation is key for why feedforward process control is necessary for the laser powder bed fusion process. Feedback process control schemes will not be able to mitigate defect causes from future layers, whereas feedforward control approaches are able to predict onset of flaws caused by subsequent layers and take appropriate action.

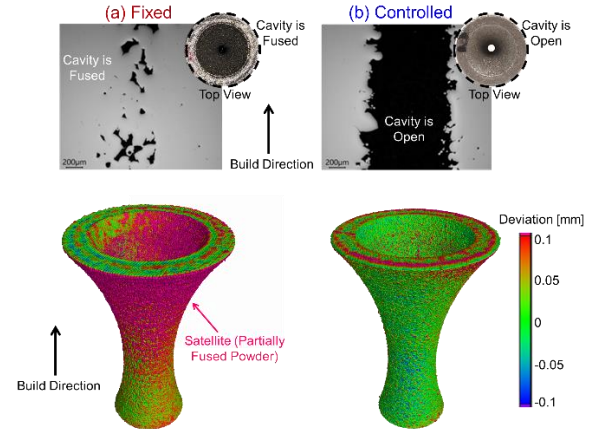


**FIGURE 12:** (TOP) OPTICAL CROSS-SECTION MICROGRAPHS. (BOTTOM) NOMINAL-TO-ACTUAL X-RAY CT DIMENSIONAL ANALYSIS OF THE VASE-SHAPED PARTS.

### 4. CONCLUSION

We developed and implemented a model-based feedforward scheme to reduce heat buildup and flaw formation in LPBF parts. The laser power and dwell time process parameters are altered layer-by-layer using insights from a physical model. This proactive approach is shown to improve surface finish, microstructure and geometric properties of multiple Inconel 718 geometries. This physics guided approach to the process optimization will reduce the need for expensive trial-and-error experiments and accelerate time-to- market of LPBF parts. In our future research, we will create an automated framework that will leverage the rapid graph theory simulations to optimize multiple process parameters. In addition, future research will focus on controlling specific flaw outcomes, such as microstructure heterogeneity.

#### **ACKNOWLEDGEMENTS**

This works was supported by the National Science Foundation (NSF) and Department of Energy (DoE) for funding his work under awards OIA-1929172, CMMI-1920245, CMMI-1739696, ECCS-2020246, PFI-TT 2044710, CMMI-1752069, CMMI-1719388, and DE-SC0021136.

All builds and data collection efforts were executed at EWI, and Ajay Krishnan's efforts was sponsored by the EWI Additive Manufacturing. The authors thank Dr. Brandon Lane of National Institute of Standards and Technology, and Dr. Abdalla Nassar, Penn State, Applied research Labs for valuable insights and discussions.

## **REFERENCES**

- [1] DebRoy, T., Wei, H. L., Zuback, J. S., Mukherjee, T., Elmer, J. W., Milewski, J. O., Beese, A. M., Wilson-Heid, A., De, A., and Zhang, W., 2018, "Additive Manufacturing of Metallic Components Process, Structure and Properties," Progress in Materials Science, **92**, pp. 112–224.
- [2] Mostafaei, A., Zhao, C., He, Y., Reza Ghiaasiaan,

- S., Shi, B., Shao, S., Shamsaei, N., Wu, Z., Kouraytem, N., Sun, T., Pauza, J., Gordon, J. V, Webler, B., Parab, N. D., Asherloo, M., Guo, Q., Chen, L., and Rollett, A. D., 2022, "Defects and Anomalies in Powder Bed Fusion Metal Additive Manufacturing," Current Opinion in Solid State and Materials Science, **26**(2), p. 100974.
- [3] Oliveira, J. P., LaLonde, A. D., and Ma, J., 2020, "Processing Parameters in Laser Powder Bed Fusion Metal Additive Manufacturing," Materials & Design, **193**, p. 108762.
- [4] Yavari, R., Smoqi, Z., Riensche, A., Bevans, B., Kobir, H., Mendoza, H., Song, H., Cole, K., and Rao, P., 2021, "Part-Scale Thermal Simulation of Laser Powder Bed Fusion Using Graph Theory: Effect of Thermal History on Porosity, Microstructure Evolution, and Recoater Crash," Materials & Design, 204, p. 109685.
- [5] Sames, W. J., List, F. A., Pannala, S., Dehoff, R. R., and Babu, S. S., 2016, "The Metallurgy and Processing Science of Metal Additive Manufacturing," International Materials Reviews, **61**(5), pp. 315–360.
- [6] Williams, R. J., Piglione, A., Rønneberg, T., Jones, C., Pham, M.-S., Davies, C. M., and Hooper, P. A., 2019, "In Situ Thermography for Laser Powder Bed Fusion: Effects of Layer Temperature on Porosity, Microstructure and Mechanical Properties," Additive Manufacturing, **30**, p. 100880.
- [7] Wang, Q., Michaleris, P., Pantano, M., Li, C., Ren, Y., and Nassar, A. R., 2022, "Part-Scale Thermal Evolution and Post-Process Distortion of Inconel-718 Builds Fabricated by Laser Powder Bed Fusion," Journal of Manufacturing Processes, 81, pp. 865–880.
- [8] Cole, K. D., Yavari, M. R., and Rao, P. K., 2020, "Computational Heat Transfer with Spectral Graph Theory: Quantitative Verification," International Journal of Thermal Sciences, **153**, p. 106383.
- [9] Cole, K. D., Riensche, A., and Rao, P. K., 2022, "Discrete Green's Functions and Spectral Graph Theory for Computationally Efficient Thermal Modeling," International Journal of Heat and Mass Transfer, **183**, p. 122112.
- [10] Yavari, R., Williams, R., Riensche, A., Hooper, P. A., Cole, K. D., Jacquemetton, L., Halliday, H. (Scott), and Rao, P. K., 2021, "Thermal Modeling in Metal Additive Manufacturing Using Graph Theory Application to Laser Powder Bed Fusion of a Large Volume Impeller," Additive Manufacturing, **41**, p. 101956.
- [11] Yavari, R., Smoqi, Z., Riensche, A., Bevans, B., Kobir, H., Mendoza, H., Song, H., Cole, K., and Rao, P., 2021, "Part-Scale Thermal Simulation of Laser Powder Bed Fusion Using Graph Theory: Effect of Thermal History on Porosity,

- Microstructure Evolution, and Recoater Crash," Materials & Design, **204**, p. 109685. Riensche, A., Severson, J., Yavari, R., Piercy, N. L.,
- [12] Riensche, A., Severson, J., Yavari, R., Piercy, N. L., Cole, K. D., and Rao, P., 2022, "Thermal Modeling of Directed Energy Deposition Additive Manufacturing Using Graph Theory," Rapid Prototyping Journal, ahead-of-p(ahead-of-print).
- [13] Yavari, M. R., Cole, K. D., and Rao, P., 2019, "Thermal Modeling in Metal Additive Manufacturing Using Graph Theory," Journal of Manufacturing Science and Engineering, **141**(7).